

Article

Large-Scale Synthesis of Iron Ore@Biomass Derived ESBC to Degrade Tetracycline Hydrochloride for Heterogeneous Persulfate Activation

Tingting Tian^{1,2}, Xinfeng Zhu^{1,*}, Zhongxian Song¹, Xindong Li², Jinhui Zhang¹, Yanli Mao¹, Junfeng Wu¹, Wei Zhang^{3,*}  and Chaohai Wang^{1,4,*} 

¹ Henan Key Laboratory of Water Pollution Control and Rehabilitation Technology, School of Environmental and Municipal Engineering, Henan University of Urban Construction, Pingdingshan 467036, China

² School of Civil and Surveying Engineering, Jiangxi University of Science and Technology, Ganzhou 341000, China

³ School of Ecology and Environmental, Zhengzhou University, Zhengzhou 450001, China

⁴ Jiangsu Key Laboratory of Chemical Pollution Control and Resources Reuse, School of Environmental and Biological Engineering, Nanjing University of Science and Technology, Nanjing 210094, China

* Correspondence: zhuxf780@163.com (X.Z.); zhangwei88@zsu.edu.cn (W.Z.); chaohai@hncj.edu.cn (C.W.)

Abstract: Iron-based catalysts are widely used in water treatment and environmental remediation due to their abundant content in nature and their ability to activate persulfate at room temperature. Here, eggshell biochar-loaded natural iron slag (IO@ESBC) was successfully synthesized to remove tetracycline hydrochloride (TCH) by activated persulfate. The morphology, structure and chemical composition of IO@ESBC were systematically characterized. The IO@ESBC/PS process showed good performance for TCH removal. The decomposition rate constant (k) for IO@ESBC was 0.011 min^{-1} and the degradation rate was 3690 mmol/g/h in this system. With the increase of PS concentration and IO@ESBC content, the removal rate of TCH both increased. The IO@ESBC/PS process can effectively remove TCH at pH 3–9. There are different effects on TCH removal for the reason that the addition of water matrix species (humic acid, Cl^- , HCO_3^- , NO_3^- and HPO_4^{2-}). The IO@ESBC/PS system for degrading TCH was mainly controlled by both the free radical pathway ($\text{SO}_4^{\bullet-}$, $\bullet\text{OH}$ and $\text{O}_2^{\bullet-}$) and non-free radical pathway ($^1\text{O}_2$). The loading of ESBC slows down the agglomeration between iron particles, and more active sites are exposed. The removal rate of TCH was still above 75% after five cycles of IO@ESBC. This interesting investigation has provided a green route for synthesis of composite driving from waste resources, expanding its further application for environmental remediations.

Keywords: iron ore; eggshell biochar; tetracycline hydrochloride; persulfate-based advanced oxidation



Citation: Tian, T.; Zhu, X.; Song, Z.; Li, X.; Zhang, J.; Mao, Y.; Wu, J.; Zhang, W.; Wang, C. Large-Scale Synthesis of Iron Ore@Biomass Derived ESBC to Degrade Tetracycline Hydrochloride for Heterogeneous Persulfate Activation. *Catalysts* **2022**, *12*, 1345. <https://doi.org/10.3390/catal12111345>

Academic Editors: Jiangkun Du, Lie Yang and Chengdu Qi

Received: 12 October 2022

Accepted: 24 October 2022

Published: 2 November 2022

Publisher's Note: MDPI stays neutral with regard to jurisdictional claims in published maps and institutional affiliations.



Copyright: © 2022 by the authors. Licensee MDPI, Basel, Switzerland. This article is an open access article distributed under the terms and conditions of the Creative Commons Attribution (CC BY) license (<https://creativecommons.org/licenses/by/4.0/>).

1. Introduction

Tetracycline hydrochloride (TCH) belongs to the tetracycline class of antibiotics. It is widely used to treat infections in poultry, cattle, pigs, sheep and aquatic products [1]. For the large number of poultry on commercial farms, antibiotics are added directly to water, feed and aerosols [2]. However, part of the antibiotics is absorbed by animals, and the other part enters the environment through animal excrement. Different concentrations of antibiotics are released into municipal water, medical wastewater, and wastewater from livestock farms [3,4]. In particular, TCH is highly stable and cannot be removed by simple treatment, so it is of great significance to remove tetracycline hydrochloride from water [5]. There are some methods to remove pollutants from the aqueous solutions, such as adsorption [6] and coagulation [7], which could separate pollutants from water but could not remove pollutants completely [8]. Moreover, membrane technologies [9], filtration [10], and sedimentation [11] have high costs and low efficiency [12]. Therefore, it was necessary to explore effective treatment methods to remove these organic pollutants from wastewater.

Sulfate radical-based advanced oxidation processes (SR-AOPs) have been widely used because the highly reactive species produced could remove refractory pollutants present in water [13]. Reactive species include sulfate radical ($\text{SO}_4^{\bullet-}$) [14], hydroxyl radicals ($\bullet\text{OH}$) [2,7], and reactive oxygen ($\text{O}_2^{\bullet-}$) [15], as well as by the generation of non-radical singlet oxygen ($^1\text{O}_2$) [16]. SR-AOPs has the advantages of low energy consumption, a high efficiency and simple operation [17]. Today, a host of catalysts have been used and developed in SR-AOPs and exhibited good potential. Activated persulfates by transition metal are commonly used, for example iron [18], cobalt [19], manganese [20] and copper [21], among which iron is the most popular because of easy access, low costly and no secondary pollution [22]. Researchers often prepared catalysts with specific features or functions to improve the performance of catalysts by introduced some macromolecular compounds or substances rich in functional groups in the process. Therefore, the preparation process is complicated, and the cost is high. Directly using waste materials to prepare catalysts not only has low cost and simple operation, but also does not cause secondary pollution to the environment. Herein, we have directly explored a natural iron ore residue (IO) from a mining company in the city of Pingdingshan, Henan Province, China, aiming to efficiently degrade organic pollutants by activating PS in the water. However, due to its own magnetic properties, iron-based catalysts often undergo agglomeration [23]. Therefore, in order to suppress agglomeration, the researchers combined the iron material with another substance.

In recent years, the composites which consist of iron-based catalysts and carbon have often been used in SR-AOPs. The rich pore structure in carbon materials enhance the mass transport of organic pollutant molecules in the pores and channels [24], the chance of contact between pollutants and metal active sites is increased, so the removal rate of pollutants is improved [25]. There have two ways to combine iron-based catalysts and carbon, one was to derive carbon from the metal organic framework using a one-step carbonization method; such as researches used MIL-88A-derived to a magnetic iron/carbon nanorod, which successfully decolorized Rhodamine B by activated PS [26]. Others include Fe-MIL-NM₂ derived Fe/Fe₃C@NC [27], MOF MIL-53(Fe)-driven Fe@porous carbon [28], Fe (Hbidc)-driven Fe@Cs [29]. Another way to do it is to combine the iron-based catalysts with pre-prepared carbon materials to form composites. For example, the researchers prepared composite activated persulfates by loading FeCo₂S₄ onto g-C₃N₄ to degrade sulfamethoxazole [30], sawdust biochar and FeS formed FeS@BC composites to remove TC by activated PS [31]. Table S1 show some statistical results of current research about Fe–Carbon composites for pollutants removal with SR-AOPs.

Therefore, iron ore (IO) enriched in iron active sites were found, but visible aggregation limited its application, and a pore structure was required to inhibit its aggregation. Biochar was a kind of multifunctional material with large specific surface area, abundant pore structure, abundant oxygen-containing functional groups and good acid and alkali resistance [32]. The majority of the carbon materials used have either been derived from metal–organic frameworks or materials such as graphene, sludge biochar and carbon nanofibers. There were no studies using eggshell biochar (ESBC). In theory, it was feasible to load IO onto ESBC to form composite materials activated PS to remove pollutants.

In this work, a composite material IO@ESBC was formed by loading natural iron slag onto eggshell biochar. The prepared materials were characterized by different characterization methods and applied to TCH removal. The reaction conditions were optimized and the effects of common substrates in water on the IO@ESBC/PS/TCH system were explored. The possible TCH removal pathways and existing mechanisms were explored by radical quenching experiments and EPR detection, too. This study may have important technical implications on TCH removal and material innovation.

2. Results and Discussion

2.1. Characterization of the Green Synthesized IO@ESBC

In order to explore the structural characteristics of IO@ESBC, the properties of IO, ESBC and IO@ESBC were analyzed by SEM, VSM, BET, XRD and Raman.

The aggregation between iron ore particles can be observed in Figure 1a. The apparent irregular pore structure on the ESBC surface could be observed in Figure 1b. The surface of IO@ESBC could be cleared to see IO particles interspersed in the pores of ESBC (Figure 1c), which increased the spacing between IO particles and inhibiting the agglomeration between particles. To prove that the addition of ESBC could inhibit IO aggregation, room temperature magnetization vs. field curves of IO and IO@ESBC detected by magnetic properties were exhibited in Supplementary Materials Figure S1. Notably, two samples showed typical S-type. It was also showed that the saturation magnetization (M_s), coercivity (H_c), remanence (M_r) value for two samples. When the IO loaded to the ESBC, the values of M_s and M_r became smaller and the value of H_c became larger. This was because the introduction of ESBC has increased the anisotropy of IO@ESBC [33]. The changes of these three values indicated that the addition of ESBC reduces the magnetism between IO particles and prevents the IO agglomeration.

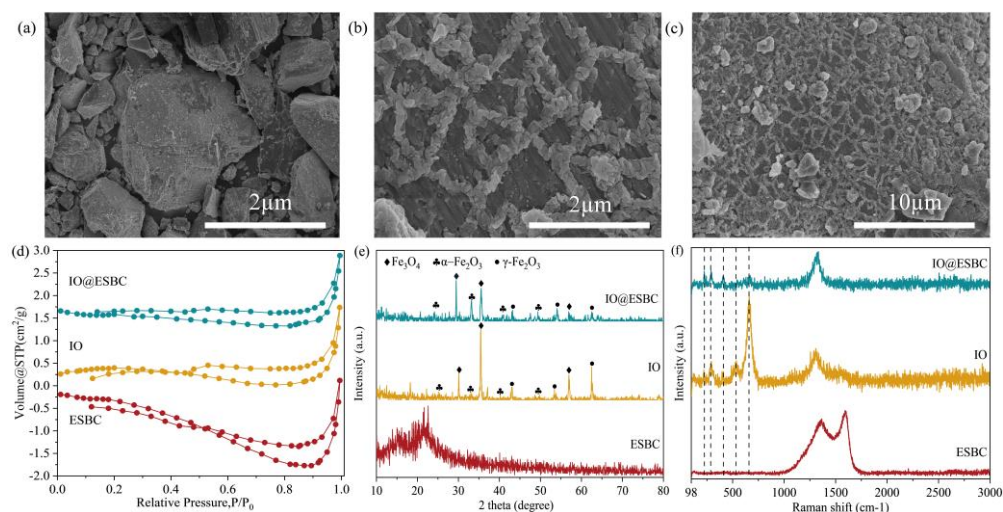


Figure 1. (a) SEM images of IO; (b) SEM images of ESBC; (c) SEM images of IO@ESBC; (d) N_2 adsorption-desorption curve of samples; (e) XRD patterns of samples; (f) Raman spectra of samples.

Figure 1d shows the N_2 adsorption-desorption isotherms of the ESBC, IO and IO@ESBC. The samples belonged to IV isotherms. The hysteresis ring in N_2 adsorption desorption curve of ESBC belonged to H_3 type, indicated that the pores on ESBC surface were slit holes formed by the accumulation of lamellar particles, which could be confirmed by Figure 1b. The hysteresis ring in N_2 adsorption desorption curve of IO moved forward when ESBC were introduced into IO, which indicated that porosity decreased significantly. The decrease of BET specific surface and total pore volume could also explain this. It further confirmed that IO successfully loaded onto the ESBC surface.

The crystallographic structures of ESBC, IO and IO@ESBC were characterized by XRD (Figure 1e). Remarkably, the XRD pattern of samples exhibited obvious diffraction peaks, indicated that the crystalline structures were better. The peak from 20° indicated amorphous structure and incomplete graphitization in ESBC. The peaks were consistent with the crystal planes of Fe_3O_4 (JCPDS 88-0866), $\alpha-Fe_2O_3$ (JCPDS 87-1165) and $\gamma-Fe_2O_3$ (JCPDS 39-1346) in IO. As was shown in Figure 1e, the characteristic peaks of IO and ESBC could be observed in the XRD patterns of IO@ESBC, which indicated that IO were successfully loaded onto ESBC.

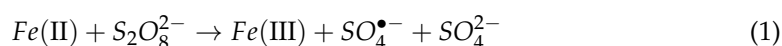
Figure 1f shows the Raman spectrum of ESBC, IO and IO@ESBC. There were two peaks in the Raman spectrum, where the D band represents disordered carbon at 1380 cm^{-1}

and the G band corresponds to graphitic carbon at 1591 cm^{-1} [34]. Compared with the IO@ESBC and ESBC, the intensity of D band and G band were smaller. It suggested that the ESBC was overwritten by IO and the IO were successfully loaded onto the ESBC. The I_D/I_G values of ESBC, IO and IO@ESBC were 0.82, 1.40 and 1.59. These values indicated that the degree of graphitization of ESBC was large, which could also be seen from the Figure 1b. However, the degree of defects of IO and IO@ESBC were larger, which could enhance the electron transfer between catalysts and PS [35,36], so the catalytic performance of the IO@ESBC was improved. The figure showed at $218.9, 292.2, 614.3\text{ cm}^{-1}$ that were characteristic peaks of $\alpha\text{-Fe}_2\text{O}_3$ [37]. At 408.3 and 660.2 cm^{-1} , which were attributable to Fe_3O_4 , and at 507.3 cm^{-1} that were assigned to $\gamma\text{-Fe}_2\text{O}_3$ [38]. The intensity of these peaks in IO@ESBC material were not significant, probably because of the IO loading in the pore structure of carbon.

The role of ESBC were analyzed in the following aspects. (1) The addition of ESBC inhibited IO agglomeration, increased the active site of catalyst, and improved the catalytic performance. (2) In the radical degradation process, ESBC as an electron transport agent caused PS decomposition to be accelerated. Since the iron active site rapidly transfers electrons to PS through special channels in ESBC, which resulted in the reactive radicals can be produced quickly. (3) In the $^1\text{O}_2$ degradation process, the introduction of ESBC increased the defects on the catalyst surface, which accelerated the electron transport between IO@ESBC and TCH, leading to the decomposition of TCH.

2.2. Catalytic Performance of IO@ESBC

TCH was hardly removed when PS was added alone, while there was a significant removal of TCH after the continued addition of IO or IO@ESBC (Figure 2a). It indicates that PS alone cannot remove pollutants and requires the addition of catalysts. In IO/PS/TCH system, the removal rate of 58.94% for TCH was due to the presence of Fe(II) and Fe(III) on the surface of IO. Fe(II) and Fe(III) could activate PS to produce $\text{SO}_4^{\bullet-}$ (Equations (1) and (2)), which could effectively remove pollutants [39]. Furthermore, the iron ions (0.5% of iron ore) would be leached from the solid phase catalysts to the solution. Thus, the experiment for contribution of released iron species on TCH removal in PS solution was conducted and shown in Figure 2a, confirming the contribution of leached iron on TCH degradation should be negligible. Nonetheless, the magnetic properties of IO made it easy to agglomerate, resulting in a reduction of active sites. The removal rate of 68.64% for TCH in ESBC/PS/TCH system, which because there were defective structures with abundant functional groups on the surface of ESBC [40]. However, ESBC were not good for recycling. The removal rate was 82.08% for TCH when IO@ESBC were added in PS/TCH system. Obviously, TCH removal rate increased by 23.14%. This indicated that IO@ESBC formed when IO were loaded onto ESBC had more active sites than IO, and the magnetic properties of IO were more conducive to recycling. In order to explore whether TCH removal was the result of adsorption of IO@ESBC or the activation of PS by IO@ESBC, the adsorption effect diagram of IO@ESBC on TCH was made (Figure 2b). The results showed that the residual amount of TCH remained at about 70.00% in 2 h as the dose of IO@ESBC increased. This indicated that the removal of TCH was mainly attributed to the activation of PS by the IO@ESBC. In addition, the XRD (Supplementary Materials Figure S2) and Raman (Supplementary Materials Figure S3) patterns of IO@ESBC after the reaction could be confirmed. In the XRD image of IO@ESBC after the reaction, it was obvious from the figure that the peak intensity of Fe_3O_4 weakened, while the peak intensity of Fe_2O_3 increased slightly. It indicated that there was a conversion of Fe_3O_4 to Fe_2O_3 during the reaction. In the Raman pattern of IO@ESBC after the reaction, the peak intensity decreases at positions 408.3 cm^{-1} and 660.2 cm^{-1} and becomes larger at other positions. It indicates that the Fe_3O_4 in the material was activated by PS and produced different levels of $\alpha\text{-Fe}_2\text{O}_3$ and $\gamma\text{-Fe}_2\text{O}_3$.



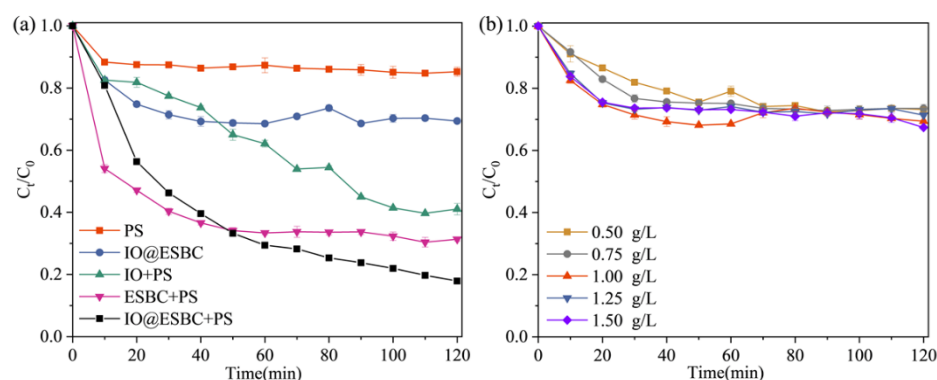


Figure 2. (a) TCH degradation by different systems; (b) Adsorption performance of TCH under different dosage of IO@ESBC. Experimental conditions: the original PS concentration of 10 mM, TCH dosage of 50 mg/L, IO@ESBC dosage of 1.25 g/L, IO dosage of 1.25 g/L, initial pH, and temperature of 25 °C.

2.3. Possible Mechanism of IO@ESBC System for TCH Removal

In order to investigate the pathway in the IO@ESBC/PS/TCH system, radical quenching experiment and EPR detection (Figure 3) were performed, respectively. TBA scavenging $\bullet\text{OH}$ ($k_{\bullet\text{OH},\text{TBA}} = (3.8\text{--}7.6 \times 10^8) \text{ M}^{-1}\text{s}^{-1}$, $k_{\text{SO}_4^{\cdot-},\text{TBA}} = (4.0\text{--}9.1 \times 10^5) \text{ M}^{-1}\text{s}^{-1}$) [41], and MeOH scavenging $\text{SO}_4^{\cdot-}$ and $\bullet\text{OH}$ ($k_{\bullet\text{OH},\text{MeOH}} = 9.7 \times 10^8 \text{ M}^{-1}\text{s}^{-1}$, $k_{\text{SO}_4^{\cdot-},\text{MeOH}} = 3.2 \times 10^6 \text{ M}^{-1}\text{s}^{-1}$) [42] were added to the system respectively. It can be seen from Figure 3a that the addition of TBA with different concentrations in the IO@ESBC/PS/TCH system had no effect on the removal of TCH. When MeOH were added, there was an inhibition effect on the removal of TCH compared with the addition of TBA, which indicated the eliminate of $\text{SO}_4^{\cdot-}$ causes the inhibition of TCH removal. The signals of DMPO- $\text{SO}_4^{\cdot-}$ and DMPO-OH were also detected in EPR (Figure 3c). The appearance of DMPO- $\text{SO}_4^{\cdot-}$ [43] was consistent with the results of quenching experiments. IO provided metal ions, involving Fe(II)-Fe(III)-Fe(II) redox cycle participate in the catalytic oxidation reaction and the PS could activated by iron ions to generate $\text{SO}_4^{\cdot-}$ (Equations (1) and (2)) [44]. Quenching experiments showed that there was no $\bullet\text{OH}$ in IO@ESBC/PS/TCH system, but the DMPO-OH [45] were also detected in the EPR. This was because PS was decomposed to produce $\text{SO}_4^{\cdot-}$ in the first stage, and $\text{SO}_4^{\cdot-}$ combines with H_2O to produce $\bullet\text{OH}$ (Equation (10)) [46]. In addition to the presence of $\text{SO}_4^{\cdot-}$ and $\bullet\text{OH}$, it was also examined whether another free radical $\text{O}_2^{\cdot-}$ plays a role in the reaction. PBQ were added to the IO@ESBC/PS/TCH system to quench $\text{O}_2^{\cdot-}$ ($k_{\text{O}_2^{\cdot-},\text{PBQ}} = 0.9\text{--}1.0 \times 10^9 \text{ M}^{-1}\text{s}^{-1}$) [47]. The presence of PBQ significantly inhibited the removal of TCH, and the higher the concentration of PBQ, the less TCH was removed (Figure 3a), which means that $\text{O}_2^{\cdot-}$ played a dominant role in the system. The typical quadruple peaks of DMPO- $\text{O}_2^{\cdot-}$ were showed in Figure 3c, which indicated the production of $\text{O}_2^{\cdot-}$ in IO@ESBC/PS/TCH system. Since the existence of oxygen vacancies has been proved in the XPS, it could be inferred that the formation of $\text{O}_2^{\cdot-}$ was mainly the electrons given by oxygen vacancies, which was consistent with the XPS O1s analysis of IO@ESBC.

$\text{O}_2^{\cdot-}$ was unstable and it will continue to react to form $^1\text{O}_2$ [48], so adding histidine to quench $^1\text{O}_2$ ($k_{^1\text{O}_2,\text{histidine}} = 8.2 \times 10^9 \text{ M}^{-1}\text{s}^{-1}$) in the system [49]. The removal of TCH received a hindrance in IO@ESBC/PS/TCH/histidine system (Figure 3b). Furthermore, the EPR spectra showed the intense triplet peaks of TEMP- $^1\text{O}_2$ in Figure 3d. The $^1\text{O}_2$ was generated in the system which because $\text{O}_2^{\cdot-}$ readily continues to react to form $^1\text{O}_2$ in an acidic environment (Equation (3)) [50]. To sum up, it could be concluded that there were two pathways that were found in this reaction by a combination of free radical quenching experiment and EPR detection. One was a free radical pathway where the major free radicals were $\text{SO}_4^{\cdot-}$, $\bullet\text{OH}$ and $\text{O}_2^{\cdot-}$; the other non-radical path was made up of $^1\text{O}_2$.

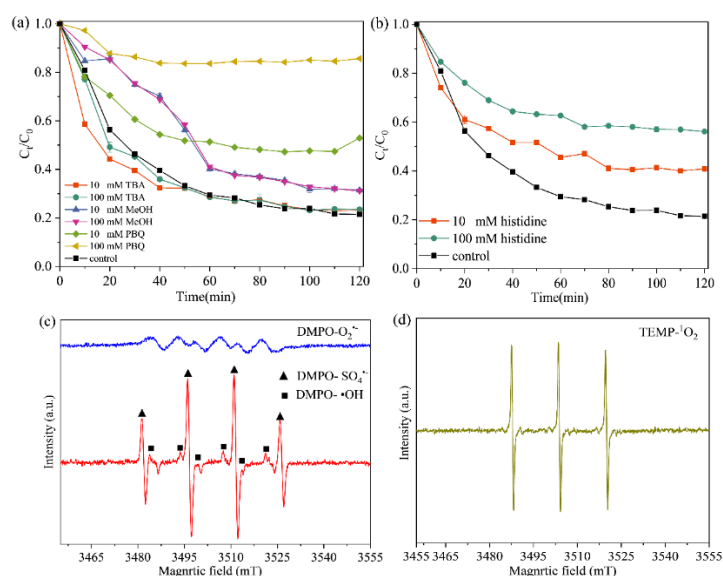


Figure 3. Quenching experiments using various scavengers in IO@ESBC/PS/TCH system (a,b); EPR spectra trapped by DMPO (100 mM) (c) and TEMP (50 μ M) (d) at 10 min. Experimental conditions: the PS concentration of 10 mM, TCH dosage of 50 mg/L, IO@ESBC dosage of 1.25 g/L, initial pH, and temperature of 25 $^{\circ}$ C.

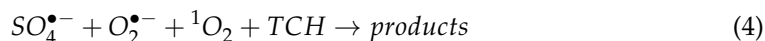
As a result, the TCH removal process in IO@ESBC/PS/TCH system was depicted in Figure 4. Notably, it can be seen that the removal rate of TCH by iron released from the catalyst is only about 1% in Figure 2a, so the contribution of leached iron ions to TCH removal is negligible. Hence, the whole reaction takes place on the surface of the catalyst. Firstly, the TCH were enriched in the surface of IO@ESBC by specific recognition and the adsorption of ESBC. The PS reached the active sites (Fe) (Equations (1) and (2)) [51], then Fe(II) captured electrons from PS which resulted in O–O bond disconnect and $\text{SO}_4^{\bullet-}$ and Fe(III) generation (Equation (1)). The Fe(III) would react with PS to generate Fe(II) (Equations (2) and (8)). Thus, a cycle of iron between the Fe(II) and Fe(III) would be formed and continued, aiming to increase the quantity of $\text{SO}_4^{\bullet-}$ in an aqueous solution. Immediately, the $\text{SO}_4^{\bullet-}$ would also react with H_2O to generate $\bullet\text{OH}$ radicals in the reaction system. The oxygen vacancy on the surface of IO@ESBC reacted with PS to form O_2^- (Equation (7)), and then $^1\text{O}_2$ produced by the recombination of O_2^- (Equation (3)). The formed reactive free radicals and $^1\text{O}_2$ were efficiently contacted and oxidized TCH on the surface of IO@ESBC (Equation (4)).



Figure 4. The proposed mechanism diagram in IO@ESBC/PS/TCH system.

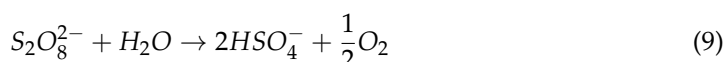
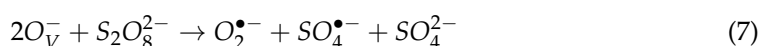
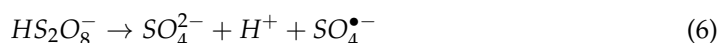
The mineralization rate (TOC) for TCH in IO@ESBC/PS/TCH system within 120 min was determined as 44.3% (Supplementary Materials Figure S6), confirming that the TCH

could not be completely mineralized. And some by-products were generated in IO@ESBC/PS/TCH system.

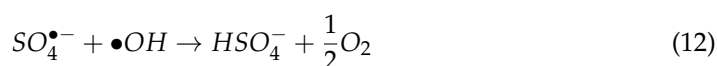
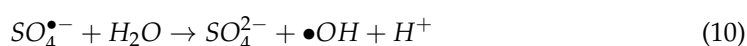


2.4. Effect of Different Conditions on TCH Removal

The actual effluent will change in pH due to environmental changes. Therefore, it was of great necessity to explore the feasibility of this reaction system in different pH environments (Figure 5a). It was clear that the removal rate of TCH in acidic environment was higher than that in alkaline and neutral environment. In general, the main free radicals were different in different acid-base environments [52]. Between pH 2 and 7, the major radicals were $SO_4^{\bullet-}$ [53]; between pH 7 and 10, the major radicals were $SO_4^{\bullet-}$ and $\bullet OH$ [54]. The reason for the higher removal of TCH in an acidic environment was the decomposition of PS and the rapid hydrolysis. Researchers thought that the acidic environment not only facilitated the decomposition of PS, but also enhanced the acid catalysis [55]. Furthermore, $O_2^{\bullet-}$ was produced in the presence of dissolved oxygen, but $O_2^{\bullet-}$ will continued to react to form 1O_2 in the acid environment (Equations (5)–(9)) [56]. Hence the presence of $SO_4^{\bullet-}$, $O_2^{\bullet-}$ and 1O_2 allowed an increased removal of TCH in an acidic environment. In contrast, the removal rate decreases when $SO_4^{\bullet-}$ and $\bullet OH$ exist simultaneously in alkaline environment. This can be explained by the following reasons. On the one hand, $\bullet OH$ will be the dominant free radical because $SO_4^{\bullet-}$ could be quenched by $\bullet OH$ in an alkaline environment (Equations (11) and (12)) [57]. However, $\bullet OH$ reacted pollutants though hydrogen abstraction reaction, which it was slower than the reaction of $SO_4^{\bullet-}$ and pollutants by electron transfer [58]. On the other hand, the metal precipitates could be generated in an alkaline environment [59], which leads to a reduction in the active sites.



In addition, the pH after the reaction tended to decrease during the reaction process (Supplementary Materials Figure S4). Moreover, they were close to original pH that it was not adjusted with H_2SO_4 or $NaOH$ in the IO@ESBC/PS/TCH system. It has already been reported that the H^+ were released by the reaction of $SO_4^{\bullet-}$ with H_2O (Equation (10)) and OH^- were consumed by the reaction with $SO_4^{\bullet-}$ (Equation (11)). Furthermore, H^+ had other sources. It was the reaction of $SO_4^{\bullet-}$ and $\bullet OH$, $S_2O_8^{2-}$ and H_2O all produced HSO_4^- , which decomposed to produce H^+ (Equations (12) and (13)) [60]. This decomposition will occur more easily in an alkaline environment, so the pH of the reaction solution decreases even at a high pH. Therefore, it was not necessary to adjust the pH for the IO@ESBC/PS/TCH system that could effectively in the practical application.



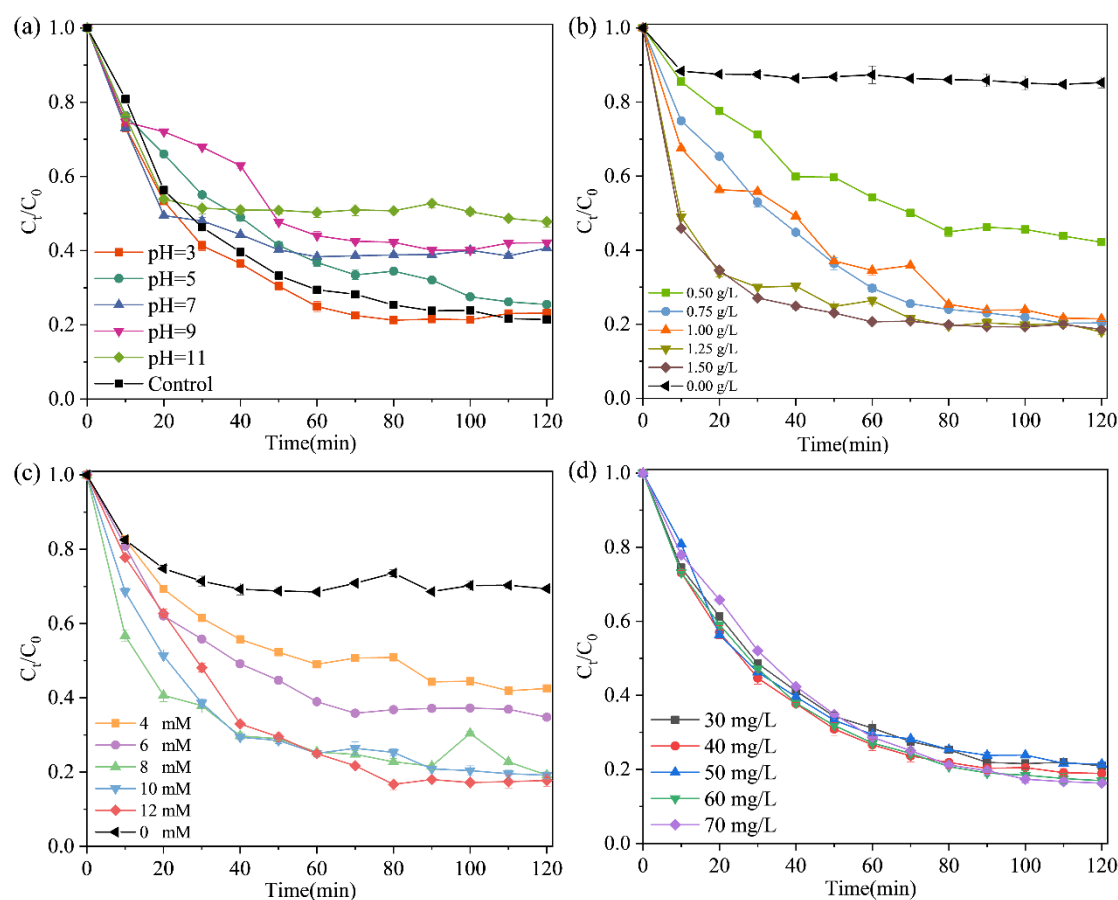
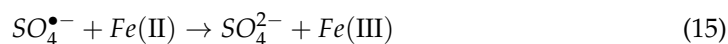
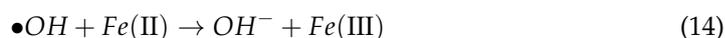


Figure 5. (a) The influence of pH (ranging from 3 to 11) on TCH removal efficiency; (b) Effect of IO@ESBC dosage (ranging from 0.50 g/L to 1.50 g/L) on TCH removal efficiency; (c) Effect of PS dosage (ranging from 4 mM to 12 mM) on TCH removal efficiency; (d) Effect of the original TCH concentration (ranging from 30 mg/L to 70 mg/L) on TCH removal efficiency.

Figure 5b showed the removal efficiency of TCH with the different IO@ESBC dosage. The residual TCH was 85.25% when the absence of IO@ESBC and the remaining amount of TCH was significantly reduced after adding IO@ESBC. The removal rate of TCH was increased (57.83%, 81.64%, 81.68%, 82.08%, 81.39%) with the increase of IO@ESBC content (0.50 g/L, 0.75 g/L, 1.00 g/L, 1.25 g/L, 1.50 g/L). This was because the amount of IO@ESBC determined the active site of Fe(II) in the reaction process [61], and the more active site of Fe(II) were more favorable to the removal of TCH to some extent. However, when the content of IO@ESBC exceeded 1.25 g/L, the removal rate of TCH was found to decrease. There were two reasons. One was that in this reaction system, not only the catalyst content will affect the removal of TCH, but also the amounts of PS [62]. Therefore, when the dosage of PS was consumed, the removal rate of TCH will not increase even if the catalyst dosage was increased. Secondly, the excess catalyst will react with $SO_4^{\bullet-}$ and $\bullet OH$, which increased the consumption of additional PS and catalyst (Equations (14) and (15)) [18], thus inhibiting the further removal of TCH. Considering the utilization efficiency, 1.25 g/L was selected as the IO@ESBC dosage in the following experiment.



The PS dosage was an important factor for the removal of TCH in the IO@ESBC/PS/TCH system because it was the source of $SO_4^{\bullet-}$. In Figure 5c, when PS was not added, the removal rate of TCH was 30.61% within 2 h. Overall, the removal rate of TCH also increased

with the increase of PS dosage, but when the PS dosage exceeded 6 mM, the removal rate of TCH basically remained the same (82.02%, 82.08%, 82.22%) with the increase of PS dose (8 mM, 10 mM, 12 mM). When the catalyst dosage was constant, PS was activated by the catalyst to produce reactive radicals for TCH removal, so the removal rate of TCH will increase with the increase of PS dosage. Nevertheless, excess PS will react with $\text{SO}_4^{\bullet-}$ (Equation (16)) [63], and the quenching reaction between $\text{SO}_4^{\bullet-}$ and $\text{SO}_4^{\bullet-}$ will occur (Equation (17)) [64], thus reducing the active site and further removal of TCH was inhibited. Thus, the PS dosage of 10 mM was considered as the most optimal dosage in the IO@ESBC/PS/TCH system.



The influence of original TCH concentration on TCH removal in IO@ESNC/PS/TCH system was investigated as described in Figure 5d. It could be seen from the graph that the removal rates of TCH were all around 80.00% at TCH concentrations ranging from 30 mg/L to 70 mg/L. This indicated that the system has good stability.

Common anions and natural organic matter in wastewater will compete for free radicals with pollutants [65]. They will affect the catalytic process and the pollutants removal process [66]. Hence, it was no wonder that explore the effect of various anions (Cl^- , HCO_3^- , NO_3^- and HPO_4^{2-}) (Figure 6) and fulvic acid in the IO@ESBC/PS/TCH system (Supplementary Materials Figure S5).

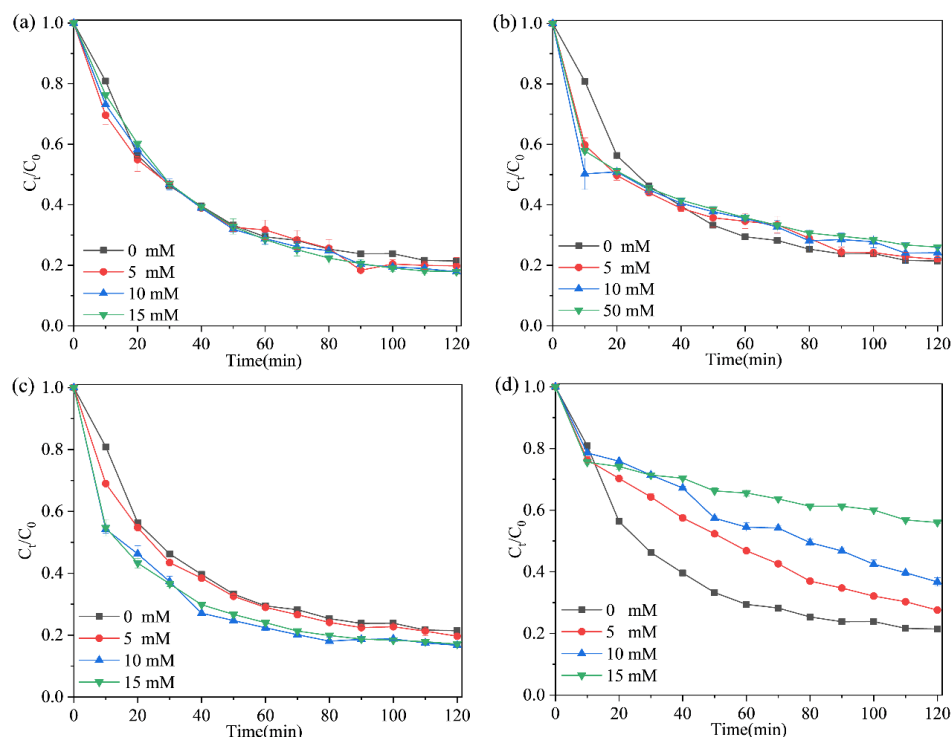
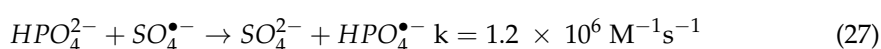
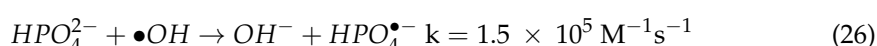
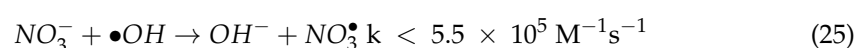
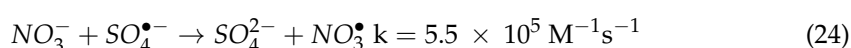
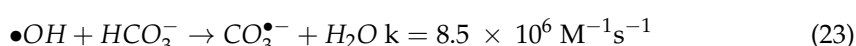
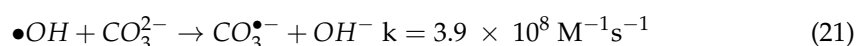
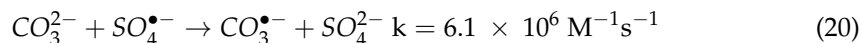
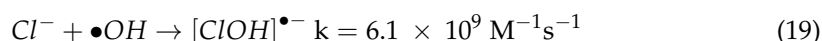
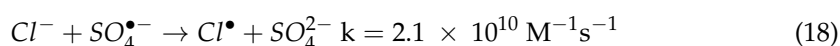


Figure 6. Effect of the anions in water (ranging from 0 mM to 15 mM) on TCH removal efficiency. (a) Cl^- ; (b) HCO_3^- ; (c) NO_3^- ; (d) HPO_4^{2-} . Experimental conditions: IO@ESBC dosage of 1.25 g/L, the original PS concentration of 10 mmol/L, TCH dosage of 50 mg/L, initial pH, and temperature of 25 °C.

In this work, it could be seen from Figure 6 that the presence of Cl^- and HCO_3^- did not show an inhibitory effect on the removal of TCH. Normally, the two anions mentioned above had an inhibitory effect on the removal of pollutants. This is because the form of reactive chlorine species ($\text{Cl}\bullet$) by the reaction of Cl^- and $\text{SO}_4^{\bullet-}$ (Equation (18)) [67] and

the form of $\text{ClOH}^{\bullet-}$ by the reaction of Cl^- and $\bullet\text{OH}$ (Equation (19)) [68], which could hardly remove pollutants [25]. On the side, the HCO_3^- could competitively react with $\bullet\text{OH}$ and $\text{SO}_4^{\bullet-}$ to generate $\text{CO}_3^{\bullet-}$ (Equations (20)–(23)), which had a low redox potential (1.63 V) [69]. These were reactions between anions and $\bullet\text{OH}$ and $\text{SO}_4^{\bullet-}$ in the reaction system, resulting in inhibition of pollutant removal. However, in IO@ESBC/PS/TCH system, there had not only $\bullet\text{OH}$ and $\text{SO}_4^{\bullet-}$ but also had $\text{O}_2^{\bullet-}$ and non-free radical paths, so the existence of Cl^- and HCO_3^- had no influence on TCH removal. Compared with the Cl^- and HCO_3^- , NO_3^- had a little boost to the removal of TCH. Although NO_3^- could also react with free radicals, their reaction rate was low (Equations (24) and (25)) [70], and a small amount of NO_3^{\bullet} could be produced to further remove TCH [71]. Contrary to the above phenomenon, the higher the concentration of HPO_4^- , the more difficult it was to remove TCH. Since the phosphate radicals were generated by the reaction $\bullet\text{OH}$, $\text{SO}_4^{\bullet-}$ and HPO_4^{2-} , which had a lower oxidation potential than $\bullet\text{OH}$, $\text{SO}_4^{\bullet-}$ (Equations (26) and (27)) [72]. This result was consistent with previous reports that phenol was removed with active substances dominated by $\bullet\text{OH}$, $\text{SO}_4^{\bullet-}$ and $^1\text{O}_2$. The removal rate of phenol decreased by 55% even though the concentration of HPO_4^{2-} was very low [73].

As a representative of natural organic matter, fulvic acid was used to explore the influence of natural organic matter in the IO@ESBC/PS/TCH system (Supplementary Materials Figure S5). Surprisingly, the removal of TCH had no effect even though the concentration of fulvic acid was high, because of the presence of the active substance ($\bullet\text{OH}$, $\text{SO}_4^{\bullet-}$, $\text{O}_2^{\bullet-}$ and $^1\text{O}_2$) in the reaction system. These active substances may counteract the competition between fulvic acid and TC for reactive substances [21].



2.5. Reusability of IO@ESBC

For heterogeneous catalysts, both catalytic performance and reusability were important [74]. XPS analysis and repeated experiments were performed to evaluate the performance of IO@ESBC in removing TCH. The Fe2p, C1s and O1s peaks clearly appeared in XPS survey spectra of samples (Figure 7a). The Fe 2p XPS of samples were shown in Figure 7b. The Fe 2p_{3/2} peak for Fe(II) and Fe(III) emerged at 710.07 and 711.57 eV [75], respectively. Fe 2p_{1/2} peak for Fe(II) and Fe(III) emerged at 723.55 and 725.31 eV [76], respectively. In addition, the satellite peak positions were 718.95 and 732.65 eV [77]. The presence of $\alpha\text{-Fe}_2\text{O}_3$, $\gamma\text{-Fe}_2\text{O}_3$ and Fe_3O_4 were confirmed by the presence of these peaks. The O 1s XPS of samples were fitted by two species (Figure 7c). It showed the spectra of O 1s that peak at 529.84 eV was assigned to Fe-O of Fe_2O_3 and Fe_3O_4 [78]. Moreover, the peak at 531.59 eV was typical of oxygen vacancies on the catalyst surface [79].

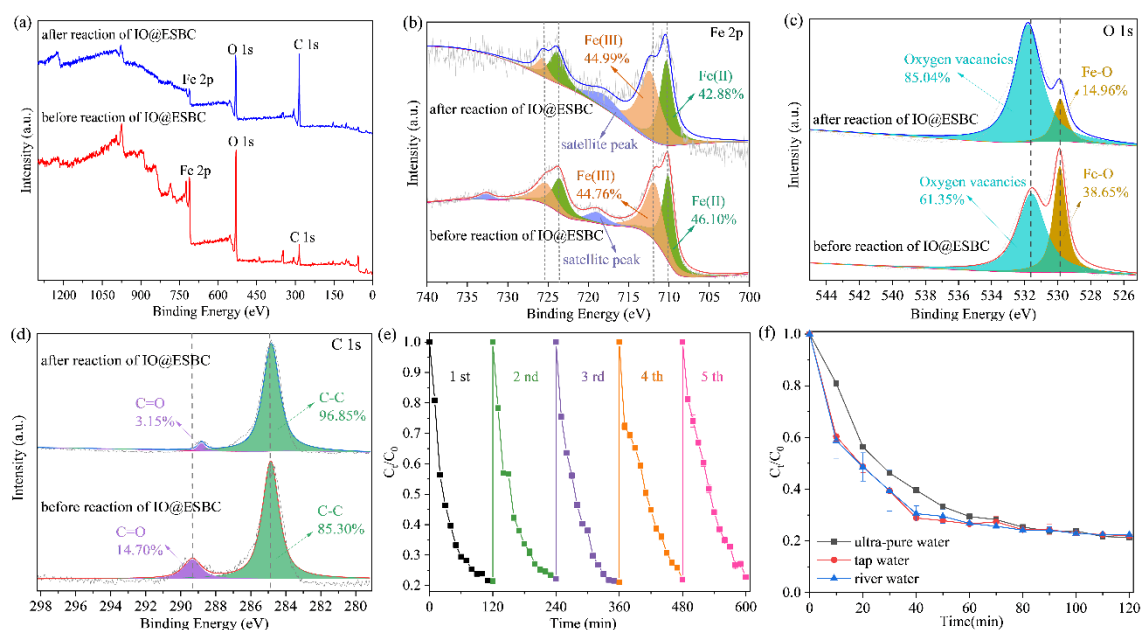


Figure 7. (a) XPS analysis of survey of IO@ESBC before and after reaction; (b) Fe 2p; (c) O 1s; (d) C 1s; (e) Recyclability of IO@ESBC; (f) Effect of different water quality in IO@ESBC/PS/TCH system. Experimental conditions: PS concentration of 10 mM, TCH dosage of 50 mg/L, IO@ESBC dosage of 1.25 g/L, and initial pH.

Figure 7d showed the spectra of C 1s that peaks at 284.86 and 289.13 eV were corresponded to the C–C bond from sp²-hybridized graphitic carbon and the carbon in C=O bond [80]. The C–C bond from sp²-hybridized graphitic carbon were the main groups for all biochar samples [81]. Obviously, the XPS diagram of IO@ESBC hardly changed before and after the reaction, indicating that the catalytic reaction did not cause the change of the catalyst structure. Further, IO@ESBC had good stability. As can be seen from Figure 7e, after IO@ESBC was reused five times, the system still maintained a high removal rate for TCH. With the increase of reaction times, the removal rate of TCH was 82.08%, 78.91%, 78.12%, 77.31%, 76.39%. The reactivity of IO@ESBC slightly decreased, which was because of the inevitable loss of catalysts during the reaction process and the increase of intermediates adsorbed on the catalysts surface during the reaction process. In order to explore the wider application of the reaction system, TCH was dissolved in river water, tap water and ultra-pure water respectively to simulate different water quality (Figure 7f). The results showed that different water quality had no effect on TCH removal, so this IO@ESBC/PS/TCH system had great potential in practical application.

3. Materials and Methods

3.1. Materials

The IO used in this study was taken from the ferromagnetic phase of a mining company in Pingdingshan City, Henan Province, China. Eggshells were taken from a bakery in Henan University of Urban Construction, Pingdingshan City, Henan Province, China. The TCH was purchased from Shanghai Aladdin Bio-Chem Technology Co., Ltd. (Shanghai, China). The reagents including PS (Na₂S₂O₈, 98%), hydrochloric acid (HCl, 36%), methanol (MeOH, 99.5%), tert-butanol (TBA, 99.5%), P-benzoquinone (PBQ, 99%), 5, 5-dimethyl-1-pyrrolidine-N-oxide (DMPO, 97%), 2,2,6,6-tetramethylpiperidone (TEMP, 99%), histidine, sodium hydroxide (NaOH, 98%), fulvic acid, sodium chloride (NaCl, 99.5%), sodium bicarbonate (NaHCO₃, ≥99.5%), sodium nitrate (NaNO₃, 99%), dipotassium hydrogen phosphate (K₂HPO₄, 98%), and sulfuric acid (H₂SO₄, 98%) were all purchased from Sinopharm Chemical Reagent Co., Ltd. (Shanghai, China). All the reagents used in this experiment were of analytical grade without further treatment.

3.2. IO@ESBC Synthesis

Iron ore sample (50 g) was passed through a 200-mesh sieve, aiming at the particles under the sieve. The obtained particles after sieving were added into 1000 mL ultrapure water, then stirred by JJ-1 precision booster electric stirrer at speed of 300 rpm. The ultrapure water in the stirring would be replaced many times until the supernatant was transparent. The iron ore sample after washing was filtered and dried at 105 °C for 12 h, then named IO.

The ESBC used in this study was obtained via slow pyrolysis of eggshells powder. Firstly, 100 g of eggshells are washed 5 times with tap water and ultra-pure water, then dried in a Desktop blast drying oven at 80 °C for 24 h. The washed eggshells are broken with a crusher, sifted through under a 200-mesh sieve. Next, the sample was calcined in a tube furnace with nitrogen flow at 150 mL/min. The pyrolysis temperature was 800 °C with 10 °C/min of the heating rate for 1 h. Then, the gained sample was dealt with HCl (2 M) until no bubbles were generated to entirely remove the calcium-containing component. The products were washed with ultra-pure water for five times and dried at 80 °C for 24 h and placed in a sealed bag.

A total of 10 g of ESBC was added to 750 mL of distilled water and stirred continuously using a JJ-1 precision booster electric stirrer (Electric mixer, MYP2011-100, Shanghai Mei Yingpu instrument and Meter Manufacturing Co., Ltd., Shanghai, China) to obtain a homogeneous suspension. Then, 50 g of IO was added and stirred for 1 h. The solid materials were filtered and rinsed with distilled water to remove the unloaded iron and other residues. Then, the solid catalyst was dried at 105 °C for 1 h and calcined at 600 °C for 1 h. The obtained sample was named IO@ESBC.

3.3. Characterization

The changes in morphologies of the samples were observed by the environmental scanning electron microscope (SEM, FEI QuANTA 200, USA). The crystal phases composition of the IO, IO@ESBC before and after reaction were measured by the D8 Advance X-ray diffractometer (XRD, Bruker, Karlsruhe, Germany) at 2θ ranging from 10° to 80°. The Raman spectroscopy (in Via confocal Raman, Renishaw Co., UK) were employed to examine the composition of the IO, IO@ESBC before and after reaction. The specific surface area and the pore size of the samples were determined by a Micromeritics TriStar II 3020 Version 3.02 analyze based on the Brunauer–Emmett–Teller (BET, Micromeritics Co., USA) method. The X-ray Photoelectron Spectroscopy (XPS, ESCALAB 250Xi, Thermo Fisher Scientific, Rockford, IL, USA) of the before and after reaction of IO@ESBC were measured by a Perkin Elmer PHI 6000C ECSA system to analyze their surface composition and elemental valence state. The free radicals (including $\bullet\text{OH}$, SO_4^- and $\text{O}_2^{\bullet-}$) and no-radical ($^1\text{O}_2$) generated in the removal process were determined by the electron spin resonance (ESR, JES-FA200, JEOL Co., Japan) spectroscopy with a dose of 100 mM DMPO and 50 μM TEMP as spin-trapping agents (Supplementary Materials Text S1). The magnetic properties of the IO and IO@ESBC were analyzed by a physical property measurement system (Quantum Design, USA).

3.4. Catalytic Activity Tests of IO@ESBC

The catalytic performance of IO@ESBC was investigated in the PS containing aqueous solution by the removal rate of TCH. For the batch experiment, a certain amount of iron ore sample was added into 250 mL conical flask containing 150 mL of TCH (50 $\text{mg}\cdot\text{L}^{-1}$) solution, followed by adding a certain dosage of PS into the mixing slurry. Then, the conical flasks containing mixing slurry were placed on a thermostatic shaker with a rotary speed of 240 rpm at a constant temperature of 25 °C. Every 10 min, 1 mL of reaction solution was quickly withdrawn from the slurry, then filtered by membrane (0.22 μm) to obtain the filtrate. Afterwards, the concentration of TCH in the filtrate was measured by UV-VIS (U7s, YOKE INSTRUMENT, Shanghai, China). The removal rate of TCH was calculated according to $(C_t - C_0)/C_0$. Nevertheless, the reaction pH was adjusted by 0.1M H_2SO_4 and 0.1 M NaOH solutions when exploring the effect of initial pH. Other experiments used

the initial pH of the reaction solution. Different quenching agents (MeOH, TBA, PBQ and histidine) were added into the reaction system of IO@ESBC/PS/TCH in the experiment to explore the free radical species.

In order to investigate the effect of the organic and inorganic anions present in the water on the reaction system, different concentrations of humic acid, NaCl, NaHCO₃, NaNO₃, and K₂HPO₄ were added to the system. The IO@ESBC sample was recycled, washed repeatedly by the deionized water, and finally dried at 105 °C in a blast drying oven. The catalyst would be reused for five times to investigate its stability and recycling performance. In order to investigate the use of catalysts in a real environment, water samples were taken from laboratory tap water and Shahe, Pingdingshan City, Henan Province, respectively. All experiments were repeated three times.

4. Conclusions

Much of the current research requires the synthesis of catalysts using chemicals. In this study, a novel material was synthesized by combining IO with ESBC, which both came from real life and did not require the use of chemicals. It was used for the removal of TCH by activating PS. The addition of ESBC not only effectively alleviates the aggregation of IO and increases the number of active sites, but also effectively adsorbs TCH and increases the chance of contact between active free radical and TCH, and finally improving the removal rate of TCH. Free radical quenching and EPR detection showed that there were not only free radical paths ($\bullet\text{OH}$, $\text{SO}_4^{\bullet-}$ and $\text{O}_2^{\bullet-}$) but also non-free radical paths ($^1\text{O}_2$) in the reaction system. The removal rate of TCH was 82.08% in 2 h with the optimized conditions of 1.25 g/L IO@ESBC, 10 mM PS, 30 mg/L TCH, initial pH. In addition, fulvic acid, Cl⁻, HCO₃⁻ and NO₃⁻ often presented in water and water quality had no influence on the reaction system, but the presence of HPO₄²⁻ had a significant inhibitory effect on TCH removal. The reusability of catalyst was also investigated and the removal rate of TCH was not affected.

Supplementary Materials: The following supporting information can be downloaded at: <https://www.mdpi.com/article/10.3390/catal12111345/s1>, Figure S1: Magnetic hysteresis loop of IO and IO@ESBC, Figure S2: The XRD pattern of IO@ESBC after reaction, Figure S3: The Raman spectra of IO@ESBC after reaction, Figure S4: The pH change record of the aqueous solution at various original pH, Figure S5: Effect of the fulvic acid (ranging from 0 mg/L to 15 mg/L) on TCH removal efficiency, Figure S6: TOC removal in IO@ESBC/PS/TCH system, Figure S7: Reaction rate curve of IO@ESBC/PS/TCH system; Table S1: Application of iron-carbon composites in water treatment; Text S1: Detection of reactive free radicals in EPR. References [26,28,29,31,82–89] are cited in the supplementary materials

Author Contributions: Conceptualization, T.T., X.Z. and Z.S.; methodology, J.Z.; software, J.W.; validation, W.Z. and X.Z.; formal analysis, C.W.; investigation, X.L.; resources, C.W.; data curation, T.T.; writing—original draft preparation, T.T.; writing—review and editing, X.Z. and Z.S.; visualization, C.W.; supervision, Y.M.; project administration, X.Z. and Y.M. All authors have read and agreed to the published version of the manuscript.

Funding: This work was financially supported by the Natural Science Foundation of Jiangsu (SBK2022041070) and the National Natural Science Foundation of China (No. 22206080).

Conflicts of Interest: The authors declare no conflict of interest.

References

1. Barbosa, M.O.; Moreira, N.F.F.; Ribeiro, A.R.; Pereira, M.F.R.; Silva, A.M.T. Occurrence and removal of organic micropollutants: An overview of the watch list of EU Decision 2015/495. *Water Res.* **2016**, *94*, 257–279. [CrossRef] [PubMed]
2. Niu, L.; Zhang, G.; Xian, G.; Ren, Z.; Wei, T.; Li, Q.; Zhang, Y.; Zou, Z. Tetracycline degradation by persulfate activated with magnetic $\gamma\text{-Fe}_2\text{O}_3/\text{CeO}_2$ catalyst: Performance, activation mechanism and degradation pathway. *Sep. Purif. Technol.* **2021**, *259*, 118156. [CrossRef]

3. Habibi, M.; Habibi-Yangjeh, A.; Sabri, M.; Chand, H.; Krishnan, V.; Wang, C. Highly impressive activation of persulfate ions by novel ZnO/CuCo₂O₄ nanostructures for photocatalytic removal of tetracycline hydrochloride under visible light. *Environ. Technol. Innov.* **2021**, *24*, 102038. [[CrossRef](#)]
4. Liu, X.; Huang, D.; Lai, C.; Zeng, G.; Qin, L.; Wang, H.; Yi, H.; Li, B.; Liu, S.; Zhang, M.; et al. Recent advances in covalent organic frameworks (COFs) as a smart sensing material. *Chem. Soc. Rev.* **2019**, *48*, 5266–5302. [[CrossRef](#)]
5. Vellingiri, K.; Philip, L.; Kim, K.-H. Metal–organic frameworks as media for the catalytic degradation of chemical warfare agents. *Coord. Chem. Rev.* **2017**, *353*, 159–179. [[CrossRef](#)]
6. Zhong, Q.; Lin, Q.; He, W.; Fu, H.; Huang, Z.; Wang, Y.; Wu, L. Study on the nonradical pathways of nitrogen-doped biochar activating persulfate for tetracycline degradation. *Sep. Purif. Technol.* **2021**, *276*, 119354. [[CrossRef](#)]
7. Hu, L.; Ren, X.; Yang, M.; Guo, W. Facet-controlled activation of persulfate by magnetite nanoparticles for the degradation of tetracycline. *Sep. Purif. Technol.* **2021**, *258*, 118014. [[CrossRef](#)]
8. Zhang, R.; Zheng, X.; Zhang, D.; Niu, X.; Ma, J.; Lin, Z.; Fu, M.; Zhou, S. Insight into the roles of endogenous minerals in the activation of persulfate by graphitized biochar for tetracycline removal. *Sci. Total Environ.* **2021**, *768*, 144281. [[CrossRef](#)]
9. Shao, F.; Wang, Y.; Mao, Y.; Shao, T.; Shang, J. Degradation of tetracycline in water by biochar supported nanosized iron activated persulfate. *Chemosphere* **2020**, *261*, 127844. [[CrossRef](#)]
10. Dang, V.C.; Tran, D.T.; Phan, A.T.; Pham, N.K.; Nguyen, V.N. Synergistic effect for the degradation of tetracycline by rGO-Co₃O₄ assisted persulfate activation. *J. Phys. Chem. Solids* **2021**, *153*, 110005. [[CrossRef](#)]
11. Huang, H.; Guo, T.; Wang, K.; Li, Y.; Zhang, G. Efficient activation of persulfate by a magnetic recyclable rape straw biochar catalyst for the degradation of tetracycline hydrochloride in water. *Sci. Total Environ.* **2021**, *758*, 143957. [[CrossRef](#)] [[PubMed](#)]
12. Liu, Z.; Gao, Z.; Wu, Q. Activation of persulfate by magnetic zirconium-doped manganese ferrite for efficient degradation of tetracycline. *Chem. Eng. J.* **2021**, *423*, 130283. [[CrossRef](#)]
13. Wu, Z.; Liang, Y.; Zou, D.; Yuan, X.; Xiao, Z.; Deng, Y.; Zhou, Y.; Jiang, L.; Qin, P. Enhanced heterogeneous activation of persulfate by Ni_xCo_{3-x}O₄ for oxidative degradation of tetracycline and bisphenol A. *J. Environ. Chem. Eng.* **2020**, *8*, 104451. [[CrossRef](#)]
14. Zhang, X.; Deng, H.; Zhang, G.; Yang, F.; Yuan, G.-E. Natural bornite as an efficient and cost-effective persulfate activator for degradation of tetracycline: Performance and mechanism. *Chem. Eng. J.* **2020**, *381*, 122717. [[CrossRef](#)]
15. Feng, Q.; Zhou, J.; Luo, W.; Ding, L.; Cai, W. Photo-Fenton removal of tetracycline hydrochloride using LaFeO₃ as a persulfate activator under visible light. *Ecotoxicol. Environ. Saf.* **2020**, *198*, 110661. [[CrossRef](#)]
16. Tang, S.; Zhao, M.; Yuan, D.; Li, X.; Zhang, X.; Wang, Z.; Jiao, T.; Wang, K. MnFe₂O₄ nanoparticles promoted electrochemical oxidation coupling with persulfate activation for tetracycline degradation. *Sep. Purif. Technol.* **2021**, *255*, 117690. [[CrossRef](#)]
17. Wang, G.; Ge, D.; Bai, L.; Dong, Y.; Bian, C.; Xu, J.; Zhu, N.; Yuan, H. Insight into the roles of electrolysis-activated persulfate oxidation in the waste activated sludge dewaterability: Effects and mechanism. *J. Environ. Manag.* **2021**, *297*, 113342. [[CrossRef](#)]
18. Ge, D.; Zhu, Y.; Li, G.; Yuan, H.; Zhu, N. Identifying the key sludge properties characteristics in Fe²⁺-activated persulfate conditioning for dewaterability amelioration and engineering implementation. *J. Environ. Manag.* **2021**, *296*, 113204. [[CrossRef](#)]
19. Syam Babu, D.; Nidheesh, P.V. Treatment of arsenite contaminated water by electrochemically activated persulfate oxidation process. *Sep. Purif. Technol.* **2022**, *282*, 119999. [[CrossRef](#)]
20. Zhang, Y.; Zhang, C.; Zhou, Z.; Wu, Y.; Xing, S. Degradation of ciprofloxacin by persulfate activation with CuO supported on Mg Al layered double hydroxide. *J. Environ. Chem. Eng.* **2021**, *9*, 106178. [[CrossRef](#)]
21. Zheng, N.; He, X.; Hu, R.; Guo, W.; Hu, Z. Co-activation of persulfate by cation and anion from FeP for advanced oxidation processes. *Appl. Catal. B Environ.* **2021**, *298*, 120505. [[CrossRef](#)]
22. Yue, X.; Guo, W.; Li, X.; Zhou, H.; Wang, R. Core-shell Fe₃O₄@MIL-101(Fe) composites as heterogeneous catalysts of persulfate activation for the removal of Acid Orange 7. *Environ. Sci. Pollut. Res.* **2016**, *23*, 15218–15226. [[CrossRef](#)] [[PubMed](#)]
23. Huang, Q.; Chen, C.; Zhao, X.; Bu, X.; Liao, X.; Fan, H.; Gao, W.; Hu, H.; Zhang, Y.; Huang, Z. Malachite green degradation by persulfate activation with CuFe₂O₄@biochar composite: Efficiency, stability and mechanism. *J. Environ. Chem. Eng.* **2021**, *9*, 105800. [[CrossRef](#)]
24. Gao, Y.; Yang, F.; Jian, H.; Zhen, K.; Zhang, P.; Tang, X.; Fu, Z.; Xu, W.; Wang, C.; Sun, H. Pyrene degradation in an aqueous system using ferrous citrate complex activated persulfate over a wide pH range. *J. Environ. Chem. Eng.* **2021**, *9*, 106733. [[CrossRef](#)]
25. Guo, J.; Gao, Q.; Yang, S.; Zheng, F.; Du, B.; Wen, S.; Wang, D. Degradation of pyrene in contaminated water and soil by Fe²⁺-activated persulfate oxidation: Performance, kinetics, and background electrolytes (Cl⁻, HCO₃⁻ and humic acid) effects. *Process Saf. Environ. Prot.* **2021**, *146*, 686–693. [[CrossRef](#)]
26. Andrew Lin, K.-Y.; Hsu, F.-K. Magnetic iron/carbon nanorods derived from a metal organic framework as an efficient heterogeneous catalyst for the chemical oxidation process in water. *RSC Adv.* **2015**, *5*, 50790–50800. [[CrossRef](#)]
27. Li, X.; Liao, F.; Ye, L.; Yeh, L. Controlled pyrolysis of MIL-88A to prepare iron/carbon composites for synergistic persulfate oxidation of phenol: Catalytic performance and mechanism. *J. Hazard. Mater.* **2020**, *398*, 122938. [[CrossRef](#)]
28. Liu, C.; Wang, Y.; Zhang, Y.; Li, R.; Meng, W.; Song, Z.; Qi, F.; Xu, B.; Chu, W.; Yuan, D.; et al. Enhancement of Fe@porous carbon to be an efficient mediator for peroxymonosulfate activation for oxidation of organic contaminants: Incorporation NH₂-group into structure of its MOF precursor. *Chem. Eng. J.* **2018**, *354*, 835–848. [[CrossRef](#)]
29. Pu, M.; Wan, J.; Zhang, F.; Brusseau, M.L.; Ye, D.; Niu, J. Insight into degradation mechanism of sulfamethoxazole by metal-organic framework derived novel magnetic Fe@C composite activated persulfate. *J. Hazard. Mater.* **2021**, *414*, 125598. [[CrossRef](#)]

30. Li, Y.; Li, J.; Pan, Y.; Xiong, Z.; Yao, G.; Xie, R.; Lai, B. Peroxymonosulfate activation on FeCo₂S₄ modified g-C₃N₄ (FeCo₂S₄-CN): Mechanism of singlet oxygen evolution for nonradical efficient degradation of sulfamethoxazole. *Chem. Eng. J.* **2020**, *384*, 123361. [[CrossRef](#)]
31. He, J.; Tang, J.; Zhang, Z.; Wang, L.; Liu, Q.; Liu, X. Magnetic ball-milled FeS@biochar as persulfate activator for degradation of tetracycline. *Chem. Eng. J.* **2021**, *404*, 126997.
32. Escobedo, E.; Cho, K.; Chang, Y.-S. Electrochemical activation of hydrogen peroxide, persulfate, and free chlorine using sacrificial iron anodes for decentralized wastewater treatment. *J. Hazard. Mater.* **2022**, *423*, 127068. [[CrossRef](#)] [[PubMed](#)]
33. Li, Y.-T.; Li, D.; Lai, L.-J.; Li, Y.-H. Remediation of petroleum hydrocarbon contaminated soil by using activated persulfate with ultrasound and ultrasound/Fe. *Chemosphere* **2020**, *238*, 124657. [[CrossRef](#)] [[PubMed](#)]
34. Nashat, M.; Mossad, M.; El-Etriby, H.K.; Gar Alalm, M. Optimization of electrochemical activation of persulfate by BDD electrodes for rapid removal of sulfamethazine. *Chemosphere* **2022**, *286*, 131579. [[CrossRef](#)] [[PubMed](#)]
35. Fagan, W.P.; Zhao, J.; Villamena, F.A.; Zweier, J.L.; Weavers, L.K. Synergistic, aqueous PAH degradation by ultrasonically-activated persulfate depends on bulk temperature and physicochemical parameters. *Ultrason. Sonochem.* **2020**, *67*, 105172. [[CrossRef](#)]
36. Zhou, X.; Lai, C.; Liu, S.; Li, B.; Qin, L.; Liu, X.; Yi, H.; Fu, Y.; Li, L.; Zhang, M.; et al. Activation of persulfate by swine bone derived biochar: Insight into the specific role of different active sites and the toxicity of acetaminophen degradation pathways. *Sci. Total Environ.* **2021**, *807*, 151059. [[CrossRef](#)]
37. Xu, Q.; Zhang, H.; Leng, H.; You, H.; Jia, Y.; Wang, S. Ultrasonic role to activate persulfate/chlorite with foamed zero-valent-iron: Sonochemical applications and induced mechanisms. *Ultrason. Sonochem.* **2021**, *78*, 105750. [[CrossRef](#)]
38. Song, H.; Li, Q.; Ye, Y.; Pan, F.; Zhang, D.; Xia, D. Degradation of cephalexin by persulfate activated with magnetic loofah biochar: Performance and mechanism. *Sep. Purif. Technol.* **2021**, *272*, 118971. [[CrossRef](#)]
39. Liu, X.; Yuan, B.; Zou, J.; Wu, L.; Dai, L.; Ma, H.; Li, K.; Ma, J. Cu(II)-enhanced degradation of acid orange 7 by Fe(II)-activated persulfate with hydroxylamine over a wide pH range. *Chemosphere* **2020**, *238*, 124533. [[CrossRef](#)]
40. Kang, Y.-G.; Chi Vu, H.; Chang, Y.-Y.; Chang, Y.-S. Fe(III) adsorption on graphene oxide: A low-cost and simple modification method for persulfate activation. *Chem. Eng. J.* **2020**, *387*, 124012. [[CrossRef](#)]
41. Zhao, Z.; Wang, L.; Fan, J.; Song, Y.; Chu, G.; Shao, L. Degradation of indigo carmine by coupling Fe(II)-activated sodium persulfate and ozone in a rotor-stator reactor. *Chem. Eng. Process. Process Intensif.* **2020**, *148*, 107791. [[CrossRef](#)]
42. Wang, H.; Deng, J.; Lu, X.; Wan, L.; Huang, J.; Liu, Y. Rapid and continuous degradation of diclofenac by Fe(II)-activated persulfate combined with bisulfite. *Sep. Purif. Technol.* **2021**, *262*, 118335. [[CrossRef](#)]
43. Ali, J.; Wenli, L.; Shahzad, A.; Ifthikar, J.; Aregay, G.G.; Shahib, I.I.; Elkhilfi, Z.; Chen, Z.; Chen, Z. Regulating the redox centers of Fe through the enrichment of Mo moiety for persulfate activation: A new strategy to achieve maximum persulfate utilization efficiency. *Water Res.* **2020**, *181*, 115862. [[CrossRef](#)] [[PubMed](#)]
44. Kang, Y.-G.; Vu, H.C.; Le, T.T.; Chang, Y.-S. Activation of persulfate by a novel Fe(II)-immobilized chitosan/alginate composite for bisphenol A degradation. *Chem. Eng. J.* **2018**, *353*, 736–745. [[CrossRef](#)]
45. Zhu, K.; Bin, Q.; Shen, Y.; Huang, J.; He, D.; Chen, W. In-situ formed N-doped bamboo-like carbon nanotubes encapsulated with Fe nanoparticles supported by biochar as highly efficient catalyst for activation of persulfate (PS) toward degradation of organic pollutants. *Chem. Eng. J.* **2020**, *402*, 126090. [[CrossRef](#)]
46. Huang, L.-Z.; Zhou, C.; Shen, M.; Gao, E.; Zhang, C.; Hu, X.-M.; Chen, Y.; Xue, Y.; Liu, Z. Persulfate activation by two-dimensional MoS₂ confining single Fe atoms: Performance, mechanism and DFT calculations. *J. Hazard. Mater.* **2020**, *389*, 122137. [[CrossRef](#)]
47. Shang, W.; Dong, Z.; Li, M.; Song, X.; Zhang, M.; Jiang, C.; Feiyun, S. Degradation of diatrizoate in water by Fe(II)-activated persulfate oxidation. *Chem. Eng. J.* **2019**, *361*, 1333–1344. [[CrossRef](#)]
48. Xu, X.; Yang, Y.; Jia, Y.; Lian, X.; Zhang, Y.; Feng, F.; Liu, Q.; Xi, B.; Jiang, Y. Heterogeneous catalytic degradation of 2,4-dinitrotoluene by the combined persulfate and hydrogen peroxide activated by the as-synthesized Fe-Mn binary oxides. *Chem. Eng. J.* **2019**, *374*, 776–786. [[CrossRef](#)]
49. Huang, S.; Li, Z.; Chen, C.; Tang, S.; Cheng, X.; Guo, X. Synergetic activation of persulfate by heat and Fe(II)-complexes for hydrolyzed polyacrylamide degradation at high pH condition: Kinetics, mechanism, and application potential for filter cake removal during cementing in CO₂ storage wells. *Sci. Total Environ.* **2020**, *713*, 136561. [[CrossRef](#)]
50. Wang, Q.; Wang, B.; Ma, Y.; Xing, S. Enhanced superoxide radical production for ofloxacin removal via persulfate activation with Cu-Fe oxide. *Chem. Eng. J.* **2018**, *354*, 473–480. [[CrossRef](#)]
51. Zhu, J.-P.; Lin, Y.-L.; Zhang, T.-Y.; Cao, T.-C.; Xu, B.; Pan, Y.; Zhang, X.-T.; Gao, N.-Y. Modelling of iohexol degradation in a Fe(II)-activated persulfate system. *Chem. Eng. J.* **2019**, *367*, 86–93. [[CrossRef](#)]
52. Wang, H.; Guo, W.; Yin, R.; Du, J.; Wu, Q.; Luo, H.; Liu, B.; Sseguya, F.; Ren, N. Biochar-induced Fe(III) reduction for persulfate activation in sulfamethoxazole degradation: Insight into the electron transfer, radical oxidation and degradation pathways. *Chem. Eng. J.* **2019**, *362*, 561–569. [[CrossRef](#)]
53. Xu, L.; Li, J.; Zeng, W.; Liu, K.; Ma, Y.; Fang, L.; Shi, C. Surfactant-assisted removal of 2,4-dichlorophenol from soil by zero-valent Fe/Cu activated persulfate. *Chin. J. Chem. Eng.* **2021**, *44*, 447–455. [[CrossRef](#)]
54. Zhang, W.; Li, X.; Yang, Q.; Wang, D.; Wu, Y.; Zhu, X.; Wei, J.; Liu, Y.; Hou, L.; Chen, C. Pretreatment of landfill leachate in near-neutral pH condition by persulfate activated Fe-C micro-electrolysis system. *Chemosphere* **2019**, *216*, 749–756. [[CrossRef](#)]
55. Dong, Y.; Wang, P.; Li, B. Fe complex immobilized on waste polypropylene fibers for fast degradation of Reactive Red 195 via enhanced activation of persulfate under LED visible irradiation. *J. Clean. Prod.* **2019**, *208*, 1347–1356. [[CrossRef](#)]

56. Li, X.; Zhou, M.; Pan, Y. Enhanced degradation of 2,4-dichlorophenoxyacetic acid by pre-magnetization Fe-C activated persulfate: Influential factors, mechanism and degradation pathway. *J. Hazard. Mater.* **2018**, *353*, 454–465. [[CrossRef](#)] [[PubMed](#)]
57. Wu, Y.; Prulho, R.; Brigante, M.; Dong, W.; Hanna, K.; Mailhot, G. Activation of persulfate by Fe(III) species: Implications for 4-tert-butylphenol degradation. *J. Hazard. Mater.* **2017**, *322*, 380–386. [[CrossRef](#)]
58. Liu, Y.; Zhang, Y.; Wang, B.; Wang, S.; Liu, M.; Wu, Y.; Lu, L.; Ren, H.; Li, H.; Dong, W.; et al. Degradation of ibuprofen in soil systems by persulfate activated with pyrophosphate chelated Fe(II). *Chem. Eng. J.* **2020**, *379*, 122145. [[CrossRef](#)]
59. Fan, J.; Gu, L.; Wu, D.; Liu, Z. Mackinawite (FeS) activation of persulfate for the degradation of p-chloroaniline: Surface reaction mechanism and sulfur-mediated cycling of iron species. *Chem. Eng. J.* **2018**, *333*, 657–664. [[CrossRef](#)]
60. Liang, C.; Liang, C.-P.; Chen, C.-C. pH dependence of persulfate activation by EDTA/Fe(III) for degradation of trichloroethylene. *J. Contam. Hydrol.* **2009**, *106*, 173–182. [[CrossRef](#)]
61. Li, X.; Guo, W.; Liu, Z.; Wang, R.; Liu, H. Fe-based MOFs for efficient adsorption and degradation of acid orange 7 in aqueous solution via persulfate activation. *Appl. Surf. Sci.* **2016**, *369*, 130–136. [[CrossRef](#)]
62. Zhu, L.; Ai, Z.; Ho, W.; Zhang, L. Core-shell Fe-Fe₂O₃ nanostructures as effective persulfate activator for degradation of methyl orange. *Sep. Purif. Technol.* **2013**, *108*, 159–165. [[CrossRef](#)]
63. Bu, L.; Shi, Z.; Zhou, S. Modeling of Fe(II)-activated persulfate oxidation using atrazine as a target contaminant. *Sep. Purif. Technol.* **2016**, *169*, 59–65. [[CrossRef](#)]
64. Yu, S.; Gu, X.; Lu, S.; Xue, Y.; Zhang, X.; Xu, M.; Qiu, Z.; Sui, Q. Degradation of phenanthrene in aqueous solution by a persulfate/percarbonate system activated with CA chelated-Fe(II). *Chem. Eng. J.* **2018**, *333*, 122–131. [[CrossRef](#)]
65. Zhen, G.; Wang, J.; Lu, X.; Su, L.; Zhu, X.; Zhou, T.; Zhao, Y. Effective gel-like floc matrix destruction and water seepage for enhancing waste activated sludge dewaterability under hybrid microwave-initiated Fe(II)-persulfate oxidation process. *Chemosphere* **2019**, *221*, 141–153. [[CrossRef](#)]
66. Chen, H.; Zhang, Z.; Feng, M.; Liu, W.; Wang, W.; Yang, Q.; Hu, Y. Degradation of 2,4-dichlorophenoxyacetic acid in water by persulfate activated with FeS (mackinawite). *Chem. Eng. J.* **2017**, *313*, 498–507. [[CrossRef](#)]
67. Zhen, G.; Lu, X.; Zhao, Y.; Chai, X.; Niu, D. Enhanced dewaterability of sewage sludge in the presence of Fe(II)-activated persulfate oxidation. *Bioresour. Technol.* **2012**, *116*, 259–265. [[CrossRef](#)]
68. Rao, Y.F.; Qu, L.; Yang, H.; Chu, W. Degradation of carbamazepine by Fe(II)-activated persulfate process. *J. Hazard. Mater.* **2014**, *268*, 23–32. [[CrossRef](#)]
69. Idrees, A.; Shan, A.; Danish, M.; Zaman, W.Q.; Mohsin, A.; Abbas, Z.; Huang, J.; Shahzad, T.; Sun, Y.; Xu, Z.; et al. Influence of preparation method on copper ferrite characteristics for the efficient degradation of trichloroethylene in persulfate activated system. *J. Environ. Chem. Eng.* **2021**, *9*, 106044. [[CrossRef](#)]
70. Han, D.; Wan, J.; Ma, Y.; Wang, Y.; Li, Y.; Li, D.; Guan, Z. New insights into the role of organic chelating agents in Fe(II) activated persulfate processes. *Chem. Eng. J.* **2015**, *269*, 425–433. [[CrossRef](#)]
71. Li, M.; Yang, X.; Wang, D.; Yuan, J. Enhanced oxidation of erythromycin by persulfate activated iron powder-H₂O₂ system: Role of the surface Fe species and synergistic effect of hydroxyl and sulfate radicals. *Chem. Eng. J.* **2017**, *317*, 103–111. [[CrossRef](#)]
72. Zhu, J.; Song, Y.; Wang, L.; Zhang, Z.; Gao, J.; Tsang, D.C.W.; Ok, Y.S.; Hou, D. Green remediation of benzene contaminated groundwater using persulfate activated by biochar composite loaded with iron sulfide minerals. *Chem. Eng. J.* **2022**, *429*, 132292. [[CrossRef](#)]
73. Sun, C.; Chen, T.; Huang, Q.; Zhan, M.; Li, X.; Yan, J. Activation of persulfate by CO₂-activated biochar for improved phenolic pollutant degradation: Performance and mechanism. *Chem. Eng. J.* **2020**, *380*, 122519. [[CrossRef](#)]
74. Han, D.; Wan, J.; Ma, Y.; Wang, Y.; Huang, M.; Chen, Y.; Li, D.; Guan, Z.; Li, Y. Enhanced decolorization of Orange G in a Fe(II)-EDDS activated persulfate process by accelerating the regeneration of ferrous iron with hydroxylamine. *Chem. Eng. J.* **2014**, *256*, 316–323. [[CrossRef](#)]
75. Xu, J.; Wang, S.; Yan, C.; Adeel Sharif, H.M.; Yang, B. Activation of sodium persulfate by TiO₂@MIL-101(Fe): Boosting the Fenton-like process by interfacial charge transfer. *Chemosphere* **2022**, *288*, 132666. [[CrossRef](#)]
76. Li, Y.; Yang, F.; Miao, S.; Wang, D.; Li, Z.; Yuan, X.; Yuan, L.; Liu, Q. Achieved deep-dewatering of dredged sediments by Fe(II) activating persulfate pretreatment: Filtrating performance and mechanistic insights. *Chem. Eng. J.* **2021**, *405*, 126847. [[CrossRef](#)]
77. Li, Y.; Wang, D.; Xu, Q.; Liu, X.; Wang, Y.; Wu, Y.; Yang, G.; Yuan, X.; Wu, Z.; Guan, R.; et al. New insight into modification of extracellular polymeric substances extracted from waste activated sludge by homogeneous Fe(II)/persulfate process. *Chemosphere* **2020**, *247*, 125804. [[CrossRef](#)]
78. Zeng, G.; Yang, R.; Fu, X.; Zhou, Z.; Xu, Z.; Zhou, Z.; Qiu, Z.; Sui, Q.; Lyu, S. Naphthalene degradation in aqueous solution by Fe(II) activated persulfate coupled with citric acid. *Sep. Purif. Technol.* **2021**, *264*, 118441. [[CrossRef](#)]
79. Rodríguez, S.; Lorenzo, D.; Santos, A.; Romero, A. Comparison of real wastewater oxidation with Fenton/Fenton-like and persulfate activated by NaOH and Fe(II). *J. Environ. Manag.* **2020**, *255*, 109926. [[CrossRef](#)]
80. Sühnhholz, S.; Kopinke, F.-D.; Mackenzie, K. Reagent or catalyst?—FeS as activator for persulfate in water. *Chem. Eng. J.* **2020**, *387*, 123804. [[CrossRef](#)]
81. Zhao, C.; Wang, J.; Chen, X.; Wang, Z.; Ji, H.; Chen, L.; Liu, W.; Wang, C.-C. Bifunctional Bi₁₂O₁₇Cl₂/MIL-100(Fe) composites toward photocatalytic Cr(VI) sequestration and activation of persulfate for bisphenol A degradation. *Sci. Total Environ.* **2021**, *752*, 141901. [[CrossRef](#)] [[PubMed](#)]

82. Wang, X.; Zhang, P.; Wang, C.; Jia, H.; Shang, X.; Tang, J.; Sun, H. Metal-rich hyperaccumulator-derived biochar as an efficient persulfate activator: Role of intrinsic metals (Fe, Mn and Zn) in regulating characteristics, performance and reaction mechanisms. *J. Hazard. Mater.* **2022**, *424*, 127225. [[CrossRef](#)] [[PubMed](#)]
83. Xie, R.; Jiang, Y.; Armutlulu, A.; Shen, Z.; Lai, B.; Wang, H. One-step fabrication of oxygen vacancy-enriched Fe@Ti/C composite for highly efficient degradation of organic pollutants through persulfate activation. *J. Colloid Interface Sci.* **2021**, *583*, 394–403. [[CrossRef](#)] [[PubMed](#)]
84. Li, X.; Rykov, A.I.; Zhang, B.; Zhang, Y.; Wang, J. Graphene encapsulated Fe_xCo_y nanocages derived from metal–organic frameworks as efficient activators for peroxymonosulfate. *Catal. Sci. Technol.* **2016**, *6*, 7486–7494. [[CrossRef](#)]
85. Chen, L.; Jiang, X.; Xie, R.; Zhang, Y.; Jin, Y.; Jiang, W. A novel porous biochar-supported Fe-Mn composite as a persulfate activator for the removal of acid red 88. *Sep. Purif. Technol.* **2020**, *250*, 117232. [[CrossRef](#)]
86. Hao, H.; Zhang, Q.; Qiu, Y.; Meng, L.; Wei, X.; Sang, W.; Tao, J. Insight into the degradation of Orange G by persulfate activated with biochar modified by iron and manganese oxides: Synergism between Fe and Mn. *J. Water Process Eng.* **2020**, *37*, 101470. [[CrossRef](#)]
87. Zhang, Y.; Zhang, B.-T.; Teng, Y.; Zhao, J.; Sun, X. Heterogeneous activation of persulfate by carbon nanofiber supported Fe₃O₄@carbon composites for efficient ibuprofen degradation. *J. Hazard. Mater.* **2021**, *401*, 123428. [[CrossRef](#)]
88. Shan, A.; Idrees, A.; Zaman, W.Q.; Abbas, Z.; Ali, M.; Rehman, M.S.U.; Hussain, S.; Danish, M.; Gu, X.; Lyu, S. Synthesis of nZVI-Ni@BC composite as a stable catalyst to activate persulfate: Trichloroethylene degradation and insight mechanism. *J. Environ. Chem. Eng.* **2021**, *9*, 104808. [[CrossRef](#)]
89. Wang, Z.; Wang, H.; Wang, Z.; Huang, D.; Qin, H.; He, Y.; Chen, M.; Zeng, G.; Xu, P. Ferrocene modified g-C₃N₄ as a heterogeneous catalyst for photo-assisted activation of persulfate for the degradation of tetracycline. *Colloids Surf. A Physicochem. Eng. Asp.* **2021**, *626*, 127024. [[CrossRef](#)]